

# Optimal Control of Medium-Voltage Drives—An Overview

Joachim Holtz, *Life Fellow, IEEE*, and Xin Qi, *Member, IEEE*

**Abstract**—Carrier modulation is the most common method for inverter control of ac drive systems. Operation at switching frequencies of several kilohertz is customary to restrain the harmonic distortion of the motor currents. Lower switching frequency is preferred for medium-voltage drives, owing to the higher switching losses of the semiconductor devices. This calls for optimizing the performance of the pulsewidth modulator. Improvements are achieved by abolishing carrier modulation with its equidistant time spacing of the voltage pulses. Optimal pulse patterns can be precalculated for every steady-state operating point of the drive. The patterns are stored in a memory of the drive system, from which they are retrieved and used for inverter control. Control at transient operation is achieved by adapting the optimal steady-state pulse patterns to the respective situation. Specific trajectories of the motor current space vector are then created by online optimization. An alternative method of online optimization relies on predicting the space vector trajectories for the next possible inverter switching states. The switching state that leads to minimum switching frequency is then selected. Optimal pulsewidth modulation reduces harmonic distortion. It permits operation at very low switching frequency and reduces the switching losses. This increases the current-carrying capability of the semiconductor devices to the extent that the power rating of an inverter approximately doubles.

**Index Terms**—Optimal control, power conversion harmonics, power converter, power quality, predictive control, pulsewidth modulation.

## I. INTRODUCTION

ADVANCES in semiconductor technology allow the fabrication of static power converters at megawatt level using medium-voltage devices such as integrated gate commutated thyristors (IGCTs) or insulated gate bipolar transistors (IGBTs). Power converters are used in ac drive systems to generate the stator currents of the drive motor. The following requirements exist:

- 1) low harmonic distortion of the motor currents for better motor efficiency and minimum torque pulsations;
- 2) low switching frequency for increased device utilization and high inverter efficiency;
- 3) fast dynamic response of the current control system.

Manuscript received July 12, 2011; revised October 4, 2011; accepted December 5, 2011. Date of publication November 29, 2012; date of current version June 21, 2013.

J. Holtz is with the University of Wuppertal, 42285 Wuppertal, Germany (e-mail: j.holtz@ieee.org).

X. Qi is with the School of Mechanical Engineering, University of Science and Technology Beijing, Beijing 100083, China (e-mail: ixin2003@gmail.com).

Color versions of one or more of the figures in this paper are available online at <http://ieeexplore.ieee.org>.

Digital Object Identifier 10.1109/TIE.2012.2230594

These requirements cannot be simultaneously satisfied when carrier-based pulsewidth modulation (PWM) is used for inverter control. This paper first discusses the mechanism of carrier modulation and explains the source of existing deficiencies. Alternative modulation methods are then analyzed, and their properties are compared and valued. Experimental results are presented.

## II. CARRIER MODULATION

Carrier modulation generates time sequences of equidistant voltage pulses. The duty cycles of the pulses at sine-triangle modulation are determined by the respective reference voltage signals per phase  $u_a^*$ ,  $u_b^*$ , and  $u_c^*$  [1], [2]. With space vector modulation, a reference voltage vector  $\mathbf{u}^*$  is sampled at equidistant time instants. A sequence is then generated of the three switching state vectors that are spatially adjacent to the reference voltage vector. Each sequence forms a modulation subcycle. A complete modulation cycle consists of two consecutive subcycles, with the respective switching state vectors being activated in reverse order. The on-durations of the switching state vectors are computed by the space vector algorithm, first published in [3]. It makes the volt-seconds of the switching sequence per subcycle equal the product  $\mathbf{u}^* \cdot (1/2f_s)$  of the sampled reference vector  $\mathbf{u}^*$  and the subcycle duration  $1/2f_s$ , where  $f_s$  is the switching frequency.

## III. OPTIMAL SUBCYCLE MODULATION

The current space vector trajectory of a carrier-modulated two-level inverter is shown in Fig. 1(a). Current distortion, both in amplitude and in phase angle, reduces whenever the applied switching state vector locates close to the back-EMF vector of the machine. The regions of minimum distortion are displaced from the directions of the switching state vectors by the phase lag  $\varphi_i$  between the reference voltage and the fundamental motor current.

Optimal subcycle modulation equalizes the current distortion within a fundamental cycle. The subcycle durations are adjusted such that constant and minimum current distortion is achieved throughout the fundamental period. This is evident from Fig. 1(b). The numerical optimization [4] is performed offline. It yields the continuous curves  $T_{\text{opt}}/T_0 = f(\arg(\mathbf{u}^*))$ , shown in Fig. 2 with the modulation index  $m$  as parameter.  $T_{\text{opt}}$  is the optimal subcycle duration at the respective phase angle  $\arg(\mathbf{u}^*)$ , and  $T_0 = 1/f_{s\text{av}}$  is the inverse of the average switching frequency. The value  $T_{\text{opt}}/T_0$  increases or reduces

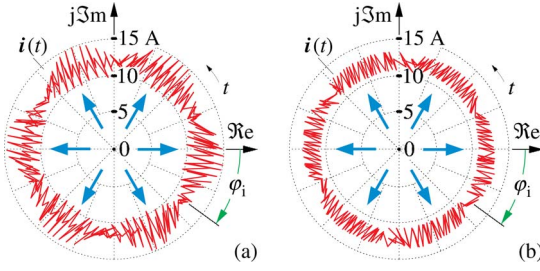


Fig. 1. Measured trajectories of the stator current space vector. (a) Space vector modulation. (b) Optimal subcycle modulation. Shown in blue are the switching state vectors of the inverter;  $\varphi_i$  is the current lag angle.

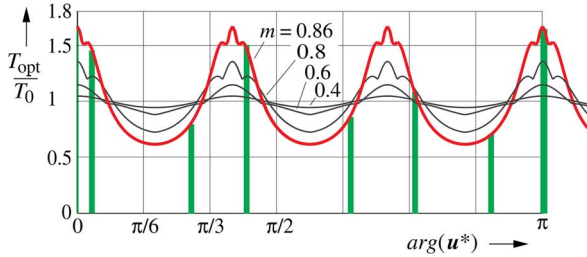


Fig. 2. Optimal subcycle durations versus fundamental phase angle. The green vertical lines mark a sequence of subcycle durations as an example for  $m = 0.86$ .

the subcycle duration with respect to its average time duration  $T_0$ . The example in Fig. 2 shows that each of the sampled values  $T_{\text{opt}}$ , represented by a green line, also determines the placement of the respective next sampling instant. Irregular subcycle durations result. A  $\pi/3$ -periodicity of  $T_{\text{opt}}/T_0$  exists in the graphs of Fig. 2 which is owed to the  $60^\circ$  spacing of the active switching state vectors.

The optimal subcycle durations are stored in a memory with the modulation index as parameter. During operation, the value  $T_{\text{opt}}/T_0$  that corresponds to the actual operating point is retrieved from the memory, and the on-durations of the switching state vectors are computed by the space vector algorithm [3]. Since frequencies  $f_s$  and  $f_1$  are not in synchronism, the sampled values of  $T_{\text{opt}}/T_0$  may be located anywhere on the time axis of diagram Fig. 2. Sampling instants then occur at different phase angles in every next fundamental cycle. Their placement shown in Fig. 2 for  $m = 0.86$  is just an example.

The effects of the optimization are seen in Fig. 1(b) for a given operating point and in Fig. 3 for the full operating region. As compared with space vector modulation, the maximum harmonic current reduces to up to 40%.

The improvement is achieved by sampling the reference voltage vector at nonperiodic time instants. The restriction of equidistant sampling is thus abolished. However, the switching state vectors are still grouped in subcycles, and their time durations still rely on the space vector algorithm. Owing to these restrictions, the modulation is suboptimal.

#### IV. SYNCHRONOUS OPTIMAL MODULATION

Following a more general approach, sequences of switching state vectors and their time durations are precalculated for

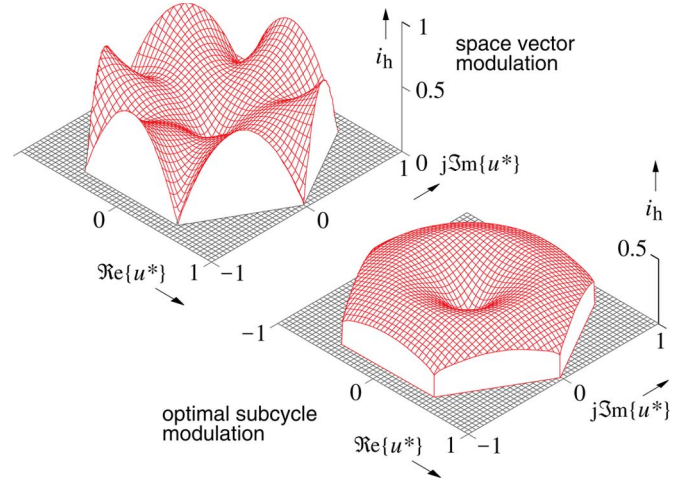


Fig. 3. Normalized harmonic current as a function of the reference voltage vector  $u^*$ , displayed in the  $z$ -axis of the complex plane.

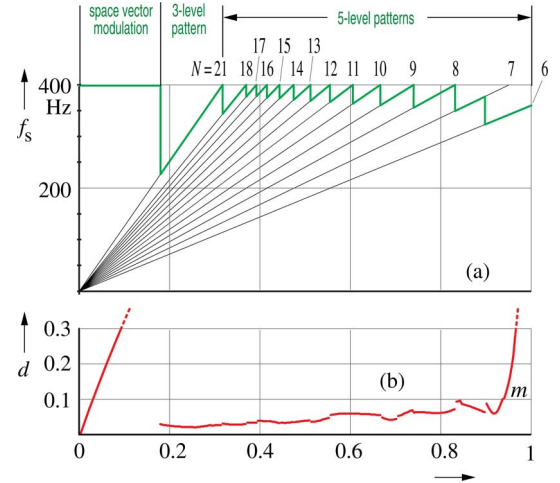


Fig. 4. Synchronous optimal modulation. Displayed versus modulation index  $m$  are (a) the switching frequency  $f_s$  and (b) the normalized current distortion  $d$ .

all values of the modulation index  $m$ . Each sequence forms a pulse pattern that gets repeated every fundamental period. The ratio  $N = f_s/f_1$ , called pulse number, is integer. This introduces synchronism between the switching frequency  $f_s$  and the fundamental frequency  $f_1$ , which makes the switching frequency vary with the modulation index as shown in Fig. 4(a).

Synchronism eliminates the subharmonic components from the generated waveforms. Half-wave and quarter-wave symmetry further nullifies all odd harmonics. The generated voltage pulses locate at irregular displacements, and a periodic volt-second balance does not exist.

The calculations are done offline, assuming steady-state operation and satisfying an optimization criterion [5]. Minimum current distortion is a preferred choice for drive applications. The resulting pulse patterns are not optimal at transient operation [6].

Selecting the switching frequency is a tradeoff between switching losses, harmonic distortion, and utilization of

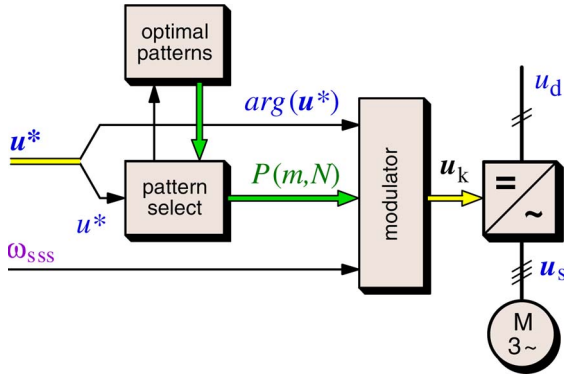


Fig. 5. Synchronous optimal modulator.

the power semiconductor devices. Choosing an upper limit  $f_{s \max} = 200$  Hz defines the required range of the modulation index  $m$  for a given pulse number  $N$ , see Fig. 4.

Current distortion  $d$  is normalized by the harmonic distortion at six-step operation, where  $d = 1$ . This way, the distortion becomes a sole characteristic of the modulation method and independent of the properties of the machine.

Harmonic distortion at PWM is inherently low at very low modulation index  $m$ . This is because a zero vector is turned on for most of the subcycle time, thus almost fully contributing to the desired output voltage of near-zero magnitude. The added active voltage vectors provide only minor corrections which generate little distortion. Current distortion  $d$  therefore starts from the origin in Fig. 4(b). Its initial portion at  $m \leq 0.18$  shows that space vector modulation is applied at  $f_{s \max}$ . Harmonic distortion is then high. This is accepted since synchronous optimal modulation would require too frequent changes of the pulse patterns in this range. Optimal modulation begins at pulse number  $N = 21$ , which covers interval  $0.18 \leq m \leq 0.32$ . The output voltage here is still low; hence, levels  $\pm u_d/2$  do not contribute to the pulse pattern, and three-level patterns result. Five-level patterns are used throughout the range  $N \leq 18$ . The distortion increases sharply in the overmodulation region.

The signal flow graph of a synchronous optimal modulator is shown in Fig. 5 [7]. An optimal pattern  $P(m, N)$  is selected by the magnitude  $u^*$  of the reference voltage vector, while its phase angle  $\arg(u^*)$  determines the switching angles. A fundamental frequency signal  $f_1$  is needed to convert the switching angles in time instants. The output vector  $u_k$  represents the generated sequence of switching states.

Combining fast dynamic control with synchronous optimal PWM poses a problem, since the optimal pulse patterns are only valid at steady-state operation [7]. Variations of the voltage reference would generate nonoptimal switching sequences, pieced together from sections of different patterns that a changing reference signal selects. The resulting volt-seconds are no longer optimal. Each change of a pattern therefore generates undesired transients in the drive motor. The example in Fig. 6(a) shows that the transient current may build up to more than twice the rated current. This would normally trigger the overcurrent protection of the inverter, and the drive system would shut down [6].

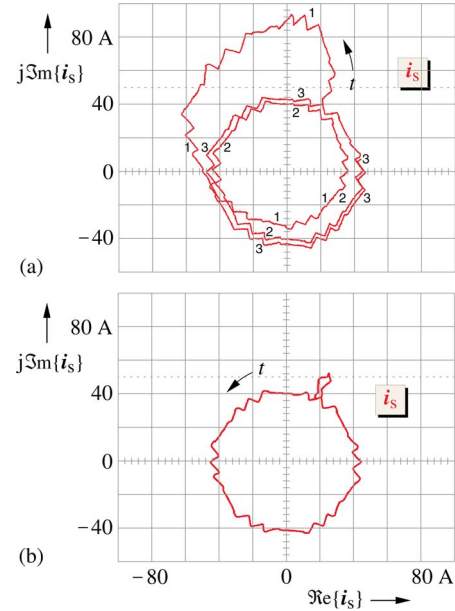


Fig. 6. Trajectories of the stator current vector at rated load, showing transients created by a change of the pulse pattern,  $f_1 = 30.5$  Hz,  $m = 0.625$ ,  $N = 6$

- (a) without trajectory tracking control,
- (b) the same process with trajectory tracking engaged; numbers 1 . . . 3 represent full cycles of rotation.

Transients also occur when the pulse pattern changes at quasi-steady state. Such transient represents an undesired operating mode of the pulsewidth modulator, which creates a dynamic modulation error. This complex variable is defined as the deviation  $d(t) = \psi_{ss}(t) - \psi_s(t)$  of the stator flux vector  $\psi_s$  from its optimal trajectory  $\psi_{ss}(t)$  [8]. The subscript  $ss$  marks a steady-state signal.

To maintain optimal control also during a dynamic process, dynamic modulation errors must be eliminated. The optimal steady-state trajectory  $\psi_{ss}(t)$  of the stator flux vector  $\psi_s$  is reconstructed in the modulator from the pulse pattern in actual use, as indicated by the signal flow graph Fig. 7. The steady-state voltage waveform  $u_{ss}(t)$  that this pattern represents is integrated to yield the optimal stator flux trajectory  $\psi_{ss}(t)$ . It serves as the reference trajectory onto which the estimated stator flux vector  $\hat{\psi}_s$  is forced. A trajectory controller is installed for this purpose. It generates additional volt-seconds by modifying the switching instants of the actual pattern and thus eliminates undesired deviations from the optimal trajectory [8]. The actual stator flux trajectory  $\hat{\psi}_s$  is estimated using a machine model.

Given its direct influence on the switching instants, the trajectory controller enforces the immediate compensation of any deviation from the optimal trajectory that the actual stator flux vector may take. This is shown in Fig. 6(b).

The almost instantaneous response of the trajectory controller suggests using it also to execute the commands of the superimposed drive control system and thus achieves fast dynamic control. This is shown in the signal flow graph in Fig. 8. The manipulating variable is the vector  $\Delta\psi_s$ . It is derived from



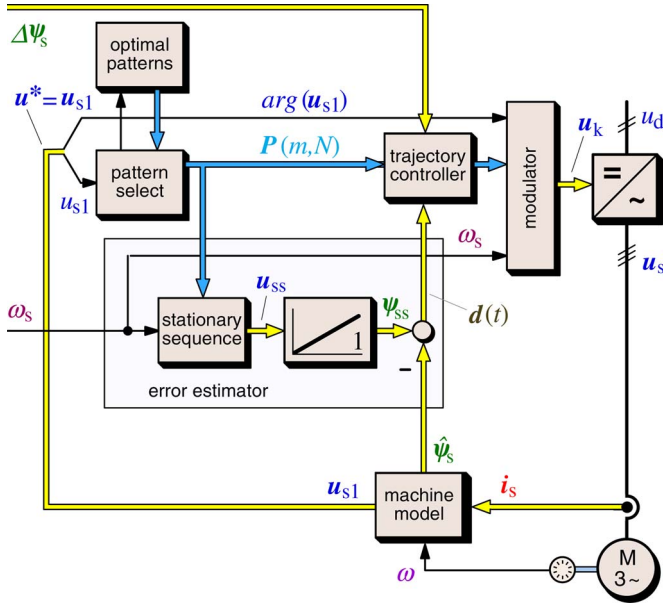


Fig. 7. Signal flow graph of a closed-loop control system with stator flux trajectory tracking. The control input to the modulator is the signal  $D\psi_s$ . The structure of the synchronous optimal pulsewidth modulator is detailed in Fig. 5.

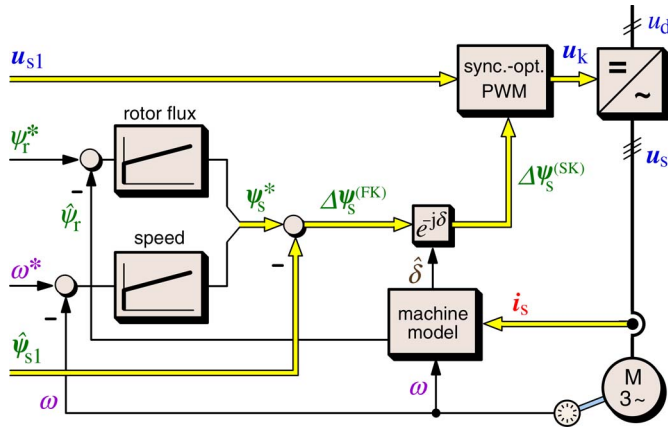


Fig. 8. Closed-loop high-dynamic speed and stator flux control, synchronous optimal modulation. Superscript <sup>FK</sup> refers to field coordinates, and <sup>SK</sup> refers to stationary coordinates. The internal structure of the element (sync. opt. PWM) is shown in Fig. 7.

the respective controllers for speed and rotor flux, according to the principle of field orientation.

The reference voltage vector  $u^*$  in Fig. 5 must be a smooth nearly sinusoidal signal, even when the drive operates in transient conditions. A signal  $u^* = u_{s1}$  is derived from the rotor model of the machine Fig. 7. Its large rotor time constant acts as a low-pass filter. An instantaneous fundamental stator voltage signal  $u_{s1}$  is thus obtained, even at transient operation.

If the estimated fundamental voltage  $u_{s1}$  was the only control input to the modulator, the drive motor would exclusively control itself. It would continue running indefinitely in any arbitrary operating point. It is only the additional control input  $\Delta\psi_s$  that can change the operating point and enforce a required dynamic response. An example is shown in the oscillogram in Fig. 9. Notwithstanding the very low switching frequency

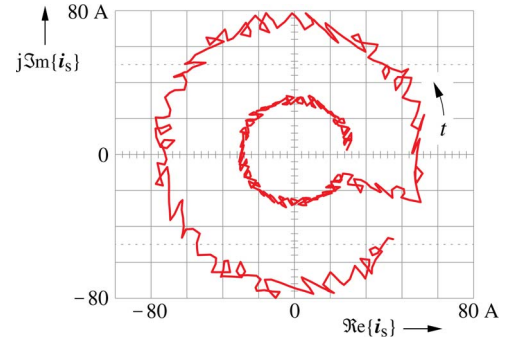


Fig. 9. Trajectory of the stator current vector  $i_s$ , recorded at a step transition from no-load operation to nominal load.

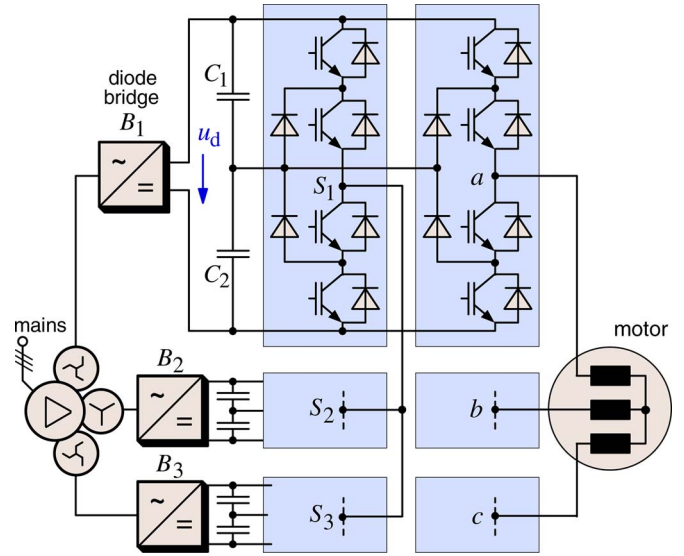


Fig. 10. Series connection per phase of two three-level half-bridges.

of 200 Hz, the trajectory controller reacts immediately to a step change of the load torque and keeps tracking the optimal trajectory.

## V. CONTROL OF MULTILEVEL INVERTERS

Multilevel inverter topologies increase the power rating of a drive system beyond the limits given by the maximum voltage ratings of the semiconductor devices. Simply using devices in series connection leads to unbalanced voltage sharing. This is avoided when each device is coupled to a capacitor that is part of the dc link circuit. Such arrangement was first proposed in [9] and [10] for thyristor inverters and later simplified for turn-off devices [11]. It keeps the device voltages constant even at switching transients.

Higher level topologies extend the voltage rating further [12]. A flying capacitor topology [13] is less suited to operate with an optimal modulation scheme. Very large capacitors would be required at low-frequency operation. Much more preferred is the series connection of two three-level half-bridges per phase [12]. Such topology acts as a five-level inverter (Fig. 10).

Synchronous optimal pulse patterns for multilevel inverter control are obtained in a similar way as previously described.

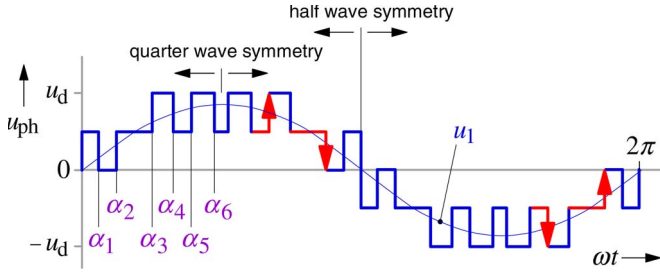


Fig. 11. Five-level phase potential  $u_{ph}$  at pulse number  $N = 6$ , defined by a set of optimal switching angles  $\alpha_i$ . The red arrows indicate the choices that have been taken at levels  $u_{ph} = \pm u_d/2$ .

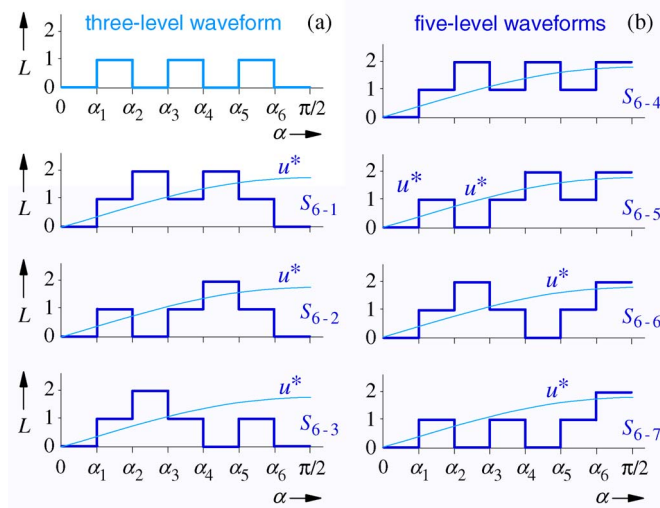


Fig. 12. Multilevel waveforms per quarter-wave: (a) three-level waveform; (b) possible structures  $S_{6,n}$  of five-level waveforms at  $N = 6$ . Logic level  $L = 1$  corresponds to  $u_d/2$  and  $L = 2$  corresponds to  $u_d$ .

While a synchronous three-level steady-state waveform is fully defined by  $N$  optimal switching angles, the optimization of higher level waveforms offers additional degrees of freedom. A five-level waveform is composed of the voltage levels  $\pm u_d$ ,  $\pm u_d/2$ , and 0 as shown in Fig. 11. Choices exist at levels  $\pm u_d/2$  as indicated by the red arrows: The inverter output potential can alternatively change in a positive or in a negative direction. This leads to a large number of different waveform structures. These are shown in Fig. 12(b) for pulse number  $N = 6$  as an example. As the pulse number increases, the number of possible structures increases exponentially [14]. There are 511 different structures at  $N = 18$ .

Given a maximum value  $f_{s \max}$  of the switching frequency, a limited range of the modulation index results for every  $N$  [15]. Fig. 4(a) indicates that the range  $0.28 \leq m \leq 0.33$  applies for  $N = 13$ . To find the optimal structure for this range, the switching angles of all existing structures are optimized. The resulting functions  $d(m)$  are shown in Fig. 13, from which the best structure is selected.

The optimal five-level patterns are subsequently decomposed in two three-level patterns to control the two three-level half-bridges. Fig. 14 shows that a pattern generator is provided for this purpose. It distributes an identical number of switching commands on the respective half-bridges. Fractional pulse

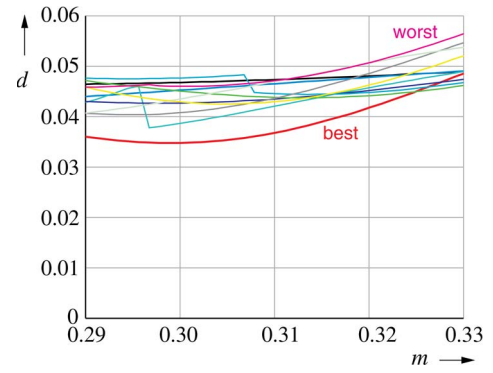


Fig. 13. Normalized harmonic distortion  $d$  at  $N = 13$ , range of 0.29–0.33 of the modulation index  $m$ , showing the worst, and the 11 best out of the totally 63 existing structures.

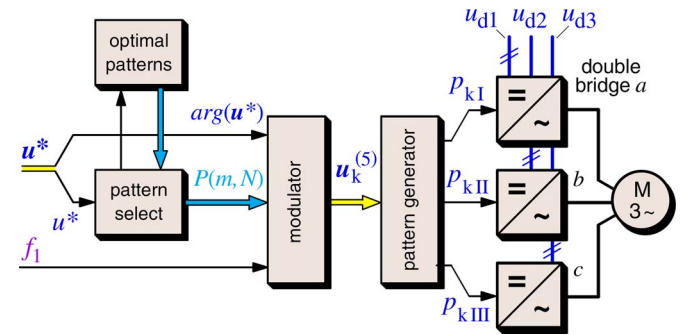


Fig. 14. Signal flow graph of an optimal five-level pulsewidth modulator to control three three-level half-bridges.

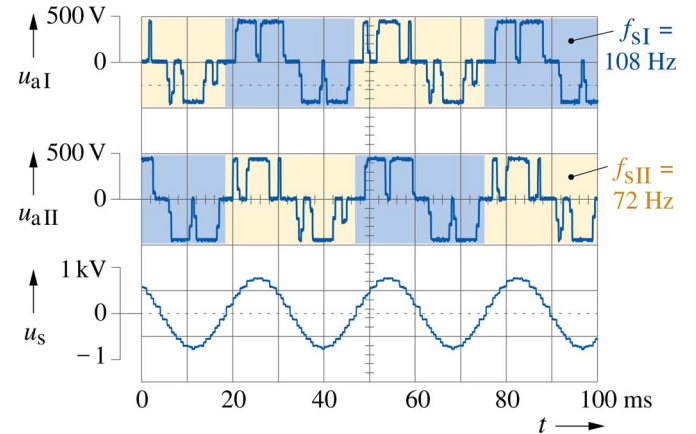


Fig. 15. Potentials of the two three-level inverters, average switching frequency  $f_s = 90$  Hz, and pulse number  $N = 2, 5$ ;  $f_1 = 36$  Hz,  $m = 0.72$ . (Lower trace) Stator voltage of the machine.

numbers  $N/2$  result if  $N$  is an odd number. As the half-bridges must receive pulse numbers of entire value, the pattern generator outputs patterns of  $N/2 + 1/2$  and  $N/2 - 1/2$ , respectively. These are periodically swapped between the two half-bridges, so as to balance the number of commutations per half-bridge [15]. Such waveforms are shown in Fig. 15 for  $N = 2.5$ .

The five-level inverter Fig. 10 consists of a series connection of two three-level half-bridges per phase. It requires a multi-winding transformer to provide separate dc voltages for each

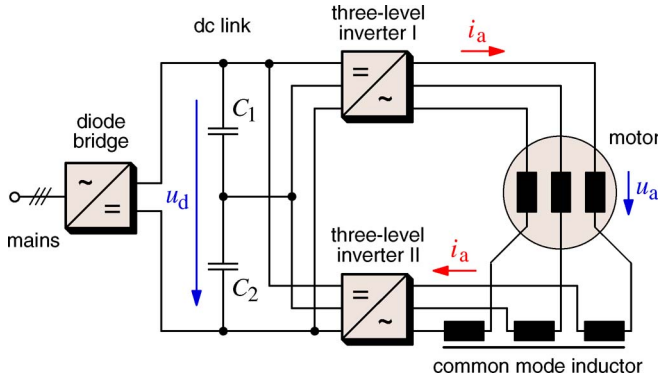


Fig. 16. Series connection of two three-level inverters.

phase. A transformerless topology may be sometimes preferred. Two three-phase inverters in Fig. 16 are series connected, feeding an open-end stator winding machine through a common mode inductor [16]. The latter serves to reducing the common mode currents that this topology produces. Common mode currents generate losses without contributing to the machine torque.

The kilovoltampere rating of the common mode inductor depends on the maximum value of the common mode flux  $\phi_0$  that the common mode voltages of the inverters generate. The maximum value  $\psi_{0 \max}$  occurs when the modulation index is maximum, and the common mode inductor must be designed for this value.

Only optimal pulse patterns creating a common mode flux less  $\psi_{0 \max}$  are then eligible for inverter control. The optimum structure must now satisfy  $\psi_0 \leq \psi_{0 \max}$  and minimum current distortion  $d$ . The structure does not exhibit the absolute minimum current distortion; however, the increase has proved to be marginal [17].

The implementation of synchronous optimal modulation tends to be inaccurate at low modulation index and higher pulse numbers  $N$ . Even minor changes of the modulation index around an operating point may cause many transitions between pulse patterns in a short time interval. The frequent transients that result become difficult to suppress by the trajectory controller.

The remedy is extending the range of pulse number  $N = 21$  to a larger interval toward the origin in Fig. 4(a) and then changing to space vector modulation. Fig. 4(b) shows that current distortion  $d$  is hardly impaired.

## VI. PREDICTIVE CONTROL

Optimum PWM based on prediction was known as early as 1982 [18]. It took the scientific community 26 years to realize the merits of this approach. Then, suddenly in 2008, intensive research on predictive control started, first continuing the investigations in inverter control [19]–[34] and, recently, also expanding to other applications [35]–[42].

The first publication [18] laid the foundation stone of this methodology, describing a predictive pulsewidth modulator for inverter control. A current error vector  $\Delta i$  as the difference between a reference current vector  $i_s^*$  and the actual

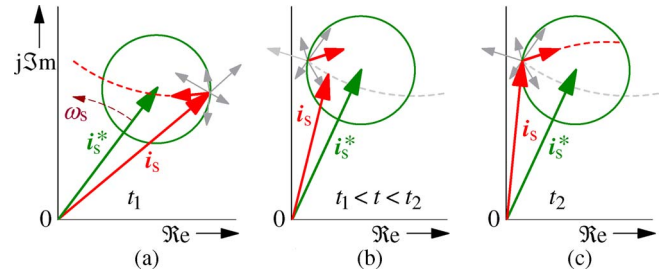


Fig. 17. Time sequence of the current vectors at predictive control.

(a) A boundary condition activates an optimum switching state.

(b) An intermediate time interval is used to predict

- the time  $t_2$  of the next boundary condition,
- the expected locations of vectors  $i_s$  and  $i_s^*$  at  $t = t_2$ ,
- based on the latter, the next optimum switching state.

(c) The predicted boundary condition activates the precalculated optimum switching state at  $t_2$  without overshoot.

current vector  $i_s$  is permanently monitored at a high repetition rate.

The switching state of the inverter is changed whenever a boundary condition occurs, i.e., when the  $\Delta i$  magnitude exceeds a given value. The incoming switching state must maintain the current vector  $i_s$  within the boundary circle. There is generally more than one switching state to serve this purpose. A selection is done by predicting the trajectories of the current vector  $i_s$  and its reference value  $i_s^*$ . The vector  $i_s$  displaces under the influence of the respective switching state. Each switching state will drive the current vector in a different direction, thus influencing the delay time until the next boundary condition occurs. A criterion to select the optimal switching state is the delay time multiplied by the number of commutations that the inverter must execute to activate that respective switching state. Maximizing this quantity leads to minimum switching frequency. Another criterion could be minimizing the switching losses.

The time sequence shown in Fig. 17 explains the details of the procedure. Control of a two-level inverter is considered for simplicity. A two-level inverter has a total of seven switching states. With the inverter holding a certain switching state, a first boundary condition occurs at time instant  $t_1$  [Fig. 17(a)]. Of the remaining six switching states, the optimal switching state is chosen. As will be shortly explained, that switching state is already known at this point of time. It is immediately activated. This avoids the current vector  $i_s$  crossing the boundary limit.

The direction that  $i_s$  will take is marked by a small red arrow in Fig. 17(a). The current vector follows the dotted trajectory toward the center of the boundary circle. The reference vector  $i_s^*$  meanwhile displaces on another trajectory which is predicted by extrapolating its recent displacement. The intermediate locations of both vectors are shown in Fig. 17(b).

In continuation, the boundary circle, being locked onto  $i_s^*$ , and the actual current vector  $i_s$  follow their respective trajectories. This leaves time for the controlling microprocessor to predict the expected displacements of the boundary circle and of  $i_s$ . The spatial location of  $i_s$  at its next intersection with the boundary circle is a target point. It will be reached at  $t_2$  as shown in Fig. 17(c). Still at  $t < t_2$ , all possible



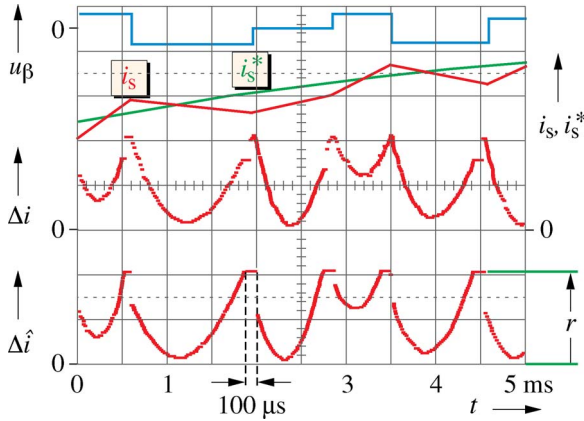


Fig. 18. Predictive control, waveforms at 170-Hz switching frequency (graph taken from [18]), and  $r$ , the radius of the boundary circle.

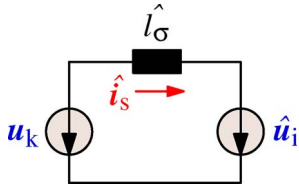


Fig. 19. Simplified machine model.

trajectories are predicted on which the current vector may continue moving beyond the target point at  $t > t_2$ . The trajectory that best satisfies the optimum criterion defines the next switching state. Its identification is completed before time instant  $t_2$ .

The oscillogram in Fig. 18 confirms that the waveform  $\Delta\hat{i}$  of the predicted error leads the actual error  $\Delta i$  in time. The current error never exceeds the radius of the boundary circle (indicated by  $r$  in Fig. 18), since the inverter switching commands are obtained by prediction. Using the measured current signals instead would introduce delays and, hence, current overshoot. Another advantage is that the current acquisition rate can be drastically reduced.

The signals in Fig. 18 are obtained as A/D-converted outputs from the controlling microprocessor. Updating the output signals discontinues whenever the predicted error signal  $\Delta\hat{i}$  indicates an imminent boundary condition. A high priority interrupt then diverts the processor activity to predicting the time instant  $t_2$  of the next boundary condition and the six possible trajectories  $\hat{i}_s(t > t_2)$  and, from these, the next optimum switching state. The calculations are completed in about 100  $\mu s$  in a standard signal processor well before the boundary condition occurs. The processor subsequently resumes its periodic output, and signals  $\Delta i$  and  $\Delta\hat{i}$  reappear in the oscillogram in Fig. 18.

Fig. 19 shows that a simplified model of the drive motor is used for the prediction of the current vector  $\hat{i}_s$ . It consists of the estimated back-EMF vector  $\hat{u}_i$  and leakage inductance  $\hat{l}_\sigma$ . The vector  $\hat{u}_k$  represents the respective switching states for which predictions are made. The simplified model is inaccurate, and its parameter may be wrongly set. The predicted current trajectory is then in error, the same as the estimated reference

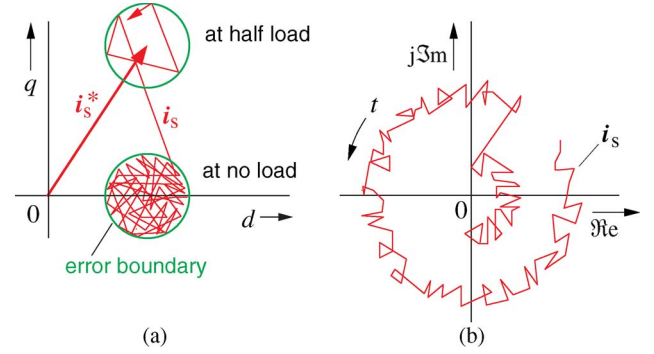


Fig. 20. Response to large-signal transients; the normalized load torque reverses between zero and 0.5 (graph taken from [18]). (a) Trajectory in field coordinates and (b) trajectory in stationary coordinates.

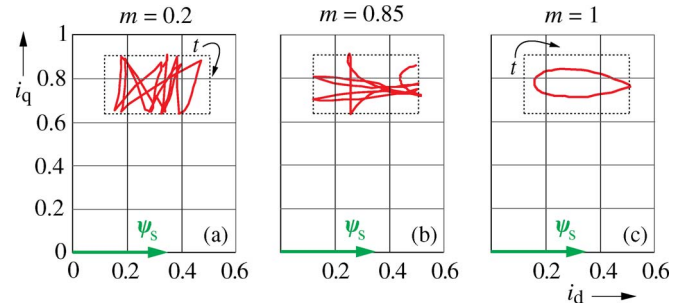


Fig. 21. Current trajectories at higher modulation index, recorded in stator flux coordinates.

vector. The result, relying on a choice between only six discrete values, is generally not affected. In a rare case of a suboptimal decision, the average objective is hardly impaired.

Achieving high dynamic performance requires a strategy to compensate large-signal errors. These may result from a commanded step change of the current reference or from a sudden load change. In either case will the current reference vector be encountered outside the boundary circle, which is the indicator of a large-signal condition. The prediction algorithm then selects a switching state that displaces the current vector into the interior of the circle within *minimum* time, disregarding the required number of commutations. An example of a large-signal transient is shown in the oscillograms in Fig. 20.

Maximum fundamental output voltage at overmodulation cannot be generated when a circular boundary is used. The oscillogram Fig. 21(b) shows that the current trajectory tends to expand in the  $d$ -axis of a stator-flux-oriented reference frame as the modulation index  $m$  increases. A boundary area that accommodates large  $d$ -axis excursions permits operating at overmodulation up to the absolute upper limit  $m = 1$  of the modulation index [43]–[45]. Six-step operation then takes place with the current trajectory assuming its maximum  $d$ -axis extension [Fig. 21(c)].

## VII. COMPARISON

Optimal subcycle modulation reduces the harmonic distortion in the upper modulation range  $m > 0.3$ . Synchronous

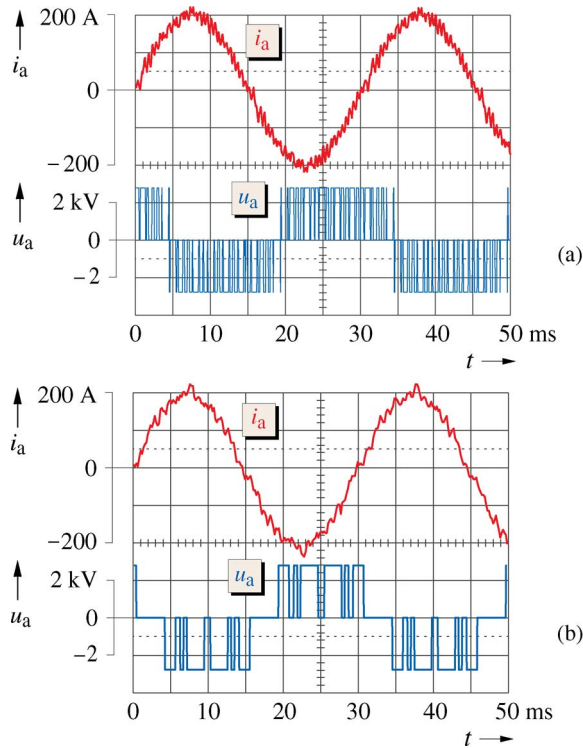


Fig. 22. Measured waveforms of the machine current and the inverter output potential, both of phase  $a$ . (a) One-kilohertz space vector modulation; (b) 200-Hz synchronous optimal modulation.

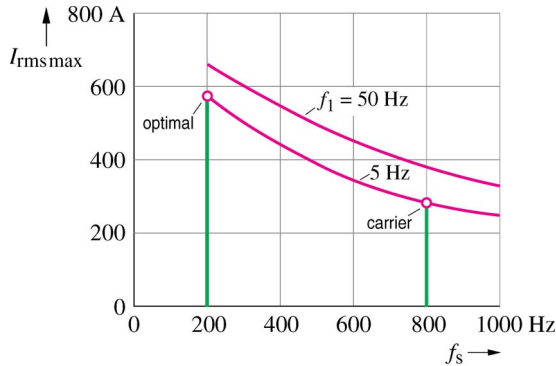


Fig. 23. Maximum rms current versus switching frequency with the fundamental frequency  $f_1$  as a parameter; EUPEC 6.5-kV 600-A IGBT; possible operating points at carrier modulation and optimal modulation are marked by circles.

optimal PWM and predictive control are best suited for applications in medium-voltage inverters. They permit reducing the switching frequency to a few 100 Hz without compromising on harmonic distortion. This is demonstrated in the oscillograms in Fig. 22.

Very low switching frequency reduces the switching losses of the devices. The example in Fig. 23 shows that a medium-voltage inverter operating at 4-kV dc-link voltage tolerates the increase of its maximum rms current from 280 to 580 A when 800-Hz carrier modulation is replaced by optimal modulation at 200-Hz switching frequency. Fig. 22 shows that the harmonic distortion is nevertheless slightly reduced.

Synchronous optimal modulation and predictive control deliver comparable results [46]. Synchronous optimal modulation

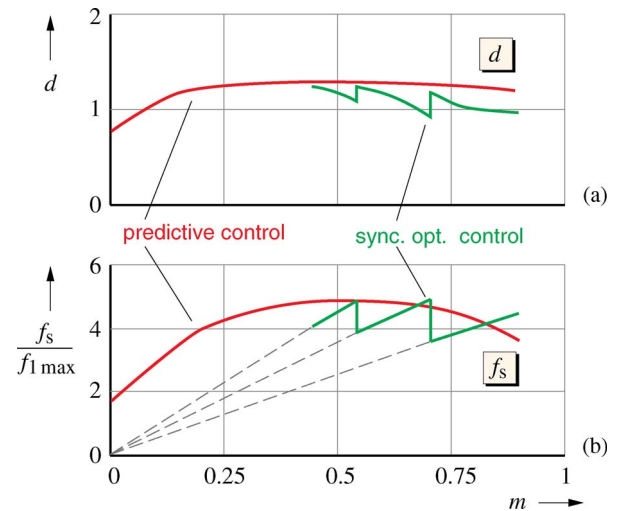


Fig. 24. Performance comparison of predictive control and synchronous optimal PWM. (a) Normalized harmonic distortion and (a) normalized switching frequency, both versus the modulation index.

generates less distortion even though the switching frequency is lower. This is shown in Fig. 24. The dynamic performance of both methods is similar, as demonstrated by a comparison of Figs. 9 and 20.

Other than predictive control, synchronous optimal modulation requires higher computing power to execute its complex algorithms. Both methods are parameter insensitive.

## VIII. CONCLUSION

Carrier modulation creates voltage pulses at regular time intervals. Three device switching transitions form a subcycle. The volt-seconds of a subcycle equal the volt-seconds of the reference signal. Two subsequent subcycles make up for a modulation cycle. Since the switching frequency is normally much higher than the fundamental frequency, almost identical volt-seconds result from a sequence of two subcycles.

Both the equidistant pulses and identical volt-seconds of the reference signal and the modulation cycle are unnecessary restrictions. Higher harmonic content of the phase currents is the consequence.

Optimal modulation methods do not have these restrictions. Optimal subcycle modulation generates irregular commutations in time but still maintains the volt-second balance per subcycle.

Synchronous optimal modulation and predictive control produce comparable harmonic distortion. The definitions of the respective algorithms support the assumption that they are indeed optimal and that better methods in terms of harmonic distortion do not exist. Both methods dispense with equidistant pulses and also with identical volt-seconds within given time intervals. Temporarily do they allow for larger volt-second differences. Deviations thus incurred are offset by delaying the next switching transition. This allows reducing the switching frequency without compromising on harmonic distortion. The utilization of the semiconductor power



devices and, consequently, the power rating of the inverter increase.

## REFERENCES

- [1] A. Schönung and H. Stemmler, "Control of a reversible three-phase motor using a static frequency inverter controlled by the suboscillation method," *Brown Boveri Rev.*, vol. 51, pp. 555–577, Aug./Sep. 1964.
- [2] J. Holtz, "Pulsewidth modulation for electronic power conversion," *Proc. IEEE*, vol. 82, no. 8, pp. 1194–1214, Aug. 1994.
- [3] A. Busse and J. Holtz, "A digital space vector modulator for the control of a three-phase power converter," (in German), in *Proc. VDE-Conf. Microelectron. Power Convert. Elect. Drives*, Darmstadt, Germany, 1982, pp. 189–195.
- [4] J. Holtz and B. Beyer, "Optimal pulsewidth modulation for AC servos and low-cost ind. drives," *IEEE Trans. Ind. Appl.*, vol. 30, no. 4, pp. 1039–1047, Jul./Aug. 1994.
- [5] G. S. Buja and G. B. Indri, "Optimal pulsewidth modulation for feeding AC motors," *IEEE Trans. Ind. Appl.*, vol. IA-13, no. 1, pp. 38–44, Jan. 1977.
- [6] J. Holtz and B. Beyer, "Fast current trajectory tracking control based on synchronous optimal pulsewidth modulation," *IEEE Trans. Ind. Appl.*, vol. 31, no. 5, pp. 1110–1120, Sep./Oct. 1995.
- [7] J. Holtz and N. Oikonomou, "Closed-loop control of medium voltage drives operated with synchronous optimal pulsewidth modulation," *IEEE Trans. Ind. Appl.*, vol. 44, no. 1, pp. 115–123, Jan./Feb. 2008.
- [8] J. Holtz and N. Oikonomou, "Synchronous optimal pulsewidth modulation and stator flux trajectory control for medium voltage drives," *IEEE Trans. Ind. Appl.*, vol. 43, no. 2, pp. 600–608, Mar./Apr. 2007.
- [9] J. Holtz, "Self-controlled inverter (three-level and multi-level)," German Patent DE 23 39 034 C2, Feb. 2, 1975, Japan (1983).
- [10] J. Holtz, "Self-commutated three-phase inverters with staircase voltage waveforms for high-power applications at low switching frequency," (in German), *Siemens Res. Dev. Surv.*, vol. 6, no. 3, pp. 164–171, 1977.
- [11] A. Nabae, I. Takahashi, and H. Akagi, "A new neutral point clamped PWM inverter," *IEEE Trans. Ind. Appl.*, vol. IA-17, no. 5, pp. 518–523, Sep. 1981.
- [12] B. Wu, *High Power Converter Systems*. Hoboken, NJ: Wiley, Mar. 2006, ISBN 0-4717-3171-4.
- [13] L. Demas, T. A. Meynard, H. Foch, and G. Gateau, "Comparative study of multilevel topologies: NPC, multicell inverter and SMC with IGBT," in *Proc. 28th Annual IEEE IECON*, 2002, pp. 828–833.
- [14] A. Rathore, J. Holtz, and T. Boller, "Synchronous optimal pulsewidth modulation for low switching frequency control of medium-voltage multilevel inverters," *IEEE Trans. Ind. Electron.*, vol. 57, no. 7, pp. 2374–2381, Jul. 2010.
- [15] T. Boller, "Optimal control of medium voltage inverters," Ph.D. dissertation, Wuppertal Univ., Wuppertal, Germany, 2011.
- [16] V. T. Somasekhar, K. Gopakumar, M. R. Baiju, K. K. Mohapatra, and L. Umanand, "A multilevel inverter system for an induction motor with open-end windings," *IEEE Trans. Ind. Electron.*, vol. 52, no. 3, pp. 824–836, Jun. 2005.
- [17] A. K. Rathore, J. Holtz, and T. Boller, "Optimal pulsewidth modulation of multilevel inverters for low switching frequency control of medium voltage high power industrial AC drives," in *Proc. IEEE Energy Convers. Congr. Exhib.*, Phoenix, AZ, Sep. 12–16, 2011, pp. 4569–4574.
- [18] J. Holts and S. Stadtfeld, "A predictive controller for the stator current vector of AC machines fed from a switched voltage source," in *Proc. IPEC*, Tokyo, Japan, 1983, pp. 1665–1675.
- [19] R. M. Kennel, A. Linder, and M. Linke, "Generalized predictive control (GPC)—Ready for use in drive applications," in *Proc. IEEE PESC*, 2001, vol. 4, pp. 1839–1844.
- [20] A. Linder and R. M. Kennel, "Direct model predictive control—A new direct predictive control strategy for electrical drives," in *Proc. Eur. Conf. Power Electron. Appl.*, 2005, [CD-ROM].
- [21] R. Vargas, P. Cortés, U. Ammann, J. Rodríguez, and J. Pontt, "Predictive control of a three-phase neutral-point-clamped inverter," *IEEE Trans. Ind. Electron.*, vol. 54, no. 5, pp. 2697–2705, Oct. 2007.
- [22] P. Cortés and J. Rodríguez, "Direct power control of an AFE using predictive control," *IEEE Trans. Power Electron.*, vol. 23, no. 5, pp. 2516–2523, Sep. 2008.
- [23] P. Antoniewicz and M. P. Kazmierkowski, "Virtual-flux-based predictive direct power of AC/DC converters with online inductance estimation," *IEEE Trans. Ind. Electron.*, vol. 55, no. 12, pp. 4381–4390, Dec. 2008.
- [24] P. Cortés, J. Rodríguez, S. Alepuz, S. Busquets-Monge, and J. Bordonau, "Finite-states model predictive control of a four-level diode-clamped inverter," in *Proc. IEEE PESC*, 2008, pp. 2203–2208.
- [25] S. Kouro, B. La Rocca, P. Cortés, S. Alepuz, B. Wu, and J. Rodríguez, "Predictive control based selective harmonic elimination with low switching frequency for multilevel converters," in *Proc. IEEE ECCE*, 2009, pp. 3130–3136.
- [26] J. Rodríguez, J. Pontt, P. Cortés, and R. Vargas, "Predictive control of a three-phase neutral point clamped inverter," *IEEE Trans. Ind. Electron.*, vol. 54, no. 5, pp. 2697–2705, Oct. 2007.
- [27] S. Kouro, P. Cortés, R. Vargas, U. Ammann, and J. Rodríguez, "Model predictive control—A simple and powerful method to control power converters," *IEEE Trans. Ind. Electron.*, vol. 56, no. 6, pp. 1826–1838, Jun. 2009.
- [28] P. Cortés, A. Wilson, S. Kouro, J. Rodríguez, and H. Abu-Rub, "Model predictive control of multilevel cascaded H-bridge inverters," *IEEE Trans. Ind. Electron.*, vol. 57, no. 8, pp. 2691–2699, Aug. 2010.
- [29] R. M. Kennel, T. Geyer, and J. C. Ramirez Martinez, "Model predictive direct current control," in *Proc. IEEE ICIT*, 2010, pp. 1808–1813.
- [30] T. Ghennam, E. Madjid Berkouk, and B. Francois, "A novel space-vector current control based on circular hysteresis areas of a three-phase neutral-point-clamped inverter," *IEEE Trans. Ind. Electron.*, vol. 57, no. 8, pp. 2669–2678, Aug. 2010.
- [31] A. Iqbal, H. Abu-Rub, P. Cortés, and J. Rodríguez, "Finite control set model predictive current control of a five-phase voltage source inverter," in *Proc. IEEE IECON*, 2010, pp. 1787–1792.
- [32] M. J. Duran, F. Barrero, and J. Prieto, "DC-bus utilization and overmodulation performance of five-phase voltage source inverters using model predictive control," in *Proc. IEEE ICIT*, 2010, pp. 1501–1506.
- [33] M. A. Perez, E. Fuentes, and J. Rodríguez, "Predictive current control of AC–AC modular multilevel converters," in *Proc. IEEE Int. Conf. Ind. Technol.*, 2010, pp. 1289–1294.
- [34] P. Cortés, J. Rodríguez, S. Vazquez, and L. G. Franquelo, "Predictive control of a three-phase UPS inverter using two steps prediction horizon," in *Proc. IEEE ICIT*, 2010, pp. 1283–1288.
- [35] Y. Fang and Y. Xing, "Design and analysis of three-phase reversible high-power-factor correction based on predictive current controller," *IEEE Trans. Ind. Electron.*, vol. 55, no. 12, pp. 4391–4397, Dec. 2008.
- [36] P. Cortés, M. P. Kazmierkowski, R. M. Kennel, D. E. Quevedo, and J. Rodríguez, "Predictive control in power electronics and drives," *IEEE Trans. Ind. Electron.*, vol. 55, no. 12, pp. 4312–4324, Dec. 2008.
- [37] J. Weigold and M. Braun, "Predictive current control using identification of current ripple," *IEEE Trans. Ind. Electron.*, vol. 55, no. 12, pp. 4346–4353, Dec. 2008.
- [38] G. Abad, M. A. Rodríguez, and J. Poza, "Three-level NPC-converter based predictive direct power control of the doubly-fed induction motor at low constant switching frequency," *IEEE Trans. Ind. Electron.*, vol. 55, no. 12, pp. 4417–4429, Dec. 2008.
- [39] H. Vargas, U. Ammann, J. Rodríguez, and J. Pontt, "A predictive strategy to control common mode voltage in loads fed by matrix converter," *IEEE Trans. Ind. Electron.*, vol. 55, no. 12, pp. 4372–4380, Dec. 2008.
- [40] E. S. de Santana, E. Bim, and W. C. do Amoral, "A predictive algorithm for controlling speed and rotor flux of induction motor," *IEEE Trans. Ind. Electron.*, vol. 55, no. 12, pp. 4398–4407, Dec. 2008.
- [41] R. Kennel, J. Rodríguez, J. Espinoza, and M. Trincado, "High performance speed control methods for electrical machines: An assessment," in *Proc. IEEE ICIT*, 2010, pp. 1793–1799.
- [42] H. Abu-Rub, J. Guzinski, J. Rodríguez, R. M. Kennel, and P. Cortés, "Predictive current controller for sensorless induction motor drive," in *Proc. IEEE ICIT*, 2010, pp. 1845–1850.
- [43] J. Holtz and E. Bube, "Field oriented asynchronous pulse-width modulation for high performance AC machine drives operating at low switching frequency," in *Conf. Rec. IEEE IAS Annu. Meeting*, Pittsburgh, PA, 1988, pp. 412–417.
- [44] J. Holtz and E. Bube, "Field oriented asynchronous pulse-width modulation for high performance AC machine drives operating at low switching frequency," *IEEE Trans. Ind. Appl.*, vol. 27, no. 3, pp. 574–581, May/Jun. 1991.
- [45] A. Khambadkone and J. Holtz, "Low switching frequency high-power inverter drive based on field-orientated pulsewidth control," in *Proc. Eur. Conf. EPE*, Florence, Italy, 1991, pp. 4/672–4/677.
- [46] T. Geyer, "A comparison of control and modulation schemes for medium-voltage drives: Emerging predictive control concepts versus field oriented control," *IEEE Trans. Ind. Appl.*, vol. 47, no. 3, pp. 1380–1389, May/Jun. 2011.



**Joachim Holtz** (M'87–SM'88–F'93–LF'11) received the Dipl.-Ing. and Ph.-D. degrees in electrical engineering from the Technical University Braunschweig, Braunschweig, Germany, in 1967 and 1969, respectively.

He was an Associate Professor in 1969 and a Full Professor and the Head of the Control Engineering Laboratory in 1971 with the Indian Institute of Technology, Madras, India. In 1972, he joined the Siemens Research Laboratories, Erlangen, Germany. From 1976 to 1998, he was a Professor and the

Head of the Electrical Machines and Drives Laboratory, Wuppertal University, Wuppertal, Germany, where he is currently a Professor Emeritus and a Consultant. He has extensively published, among others, two invited papers in the PROCEEDINGS OF THE IEEE, 12 invited papers in other IEEE journals, and 26 papers as a single author. He is a coauthor of four books and is the holder of 31 patents. He is the recipient of 16 prize paper awards.

Dr. Holtz was the Editor-in-Chief of the IEEE TRANSACTIONS ON INDUSTRIAL ELECTRONICS, a Distinguished Lecturer of the IEEE Industry Applications Society and the IEEE Industrial Electronics Society, Life AdCom member of the IEEE Industrial Electronics Society, and member of the Static Power Converter Committee of the IEEE Industry Applications Society. He was the recipient of the IEEE Industrial Electronics Society Dr. Eugene Mittelmann Achievement Award, the IEEE Industry Applications Society Outstanding Achievement Award, the IEEE Power Electronics Society William E. Newell Award, the IEEE Third Millennium Medal for outstanding contributions, the Anthony J. Hornfeck Service Award, and the IEEE Lamme Gold Medal.



**Xin Qi** (S'06–M'11) was born in Beijing, China, in 1982. He received the B.S. and Ph.D. degrees in electrical and mechanical engineering from the University of Science and Technology Beijing, Beijing, China, in 2004 and 2011, respectively.

He was a Research Assistant with the Electrical Machines and Drives Laboratory, University of Wuppertal, Wuppertal, Germany, in 2009, 2010, and June/July 2012. He is currently a Postdoctoral Research Associate with the School of Mechanical Engineering, University of Science and Technology

Beijing. His research interests include sensorless control of ac machines, online optimized pulsewidth-modulation techniques, and control strategies for inverters and ac machine drives.